energies

MDPI

Article

Effects of Biodiesel Addition on the Physical Properties and Reactivity of the Exhaust Soot Particles from Diesel Engine

Xuyang Zhang, Gang Lyu *, Chonglin Song and Yuehan Qiao

State Key Laboratory of Engines, Tianjin University, Tianjin 300072, China; zhangxu2014@tju.edu.cn (X.Z.); songchonglin@tju.edu.cn (C.S.); qiaojohn@tju.edu.cn (Y.Q.)

* Correspondence: lvg@tju.edu.cn; Tel.: +86-22-2740-6840 (ext. 8020)

Received: 22 July 2020; Accepted: 12 August 2020; Published: 14 August 2020

Abstract: The present study investigated the effects of adding 20 vol.% biodiesel to petroleum diesel (to produce a mixture termed B20) on the physical properties and reactivity of the resulting exhaust soot particles. Tests were performed at different engine loads of a constant speed, and the soot particles from the combustion of B20 and petroleum diesel fuel (DF) were collected from the engine exhaust stream. Transmission electron microscopy and Raman spectroscopy were employed for the analysis of soot morphology and nanostructure. The thermogravimetric analysis was used to determine the oxidative reactivity of the soot. For both the DF and B20 soot, increased engine loads result in soot aggregates with more compact morphology and primary soot particles with larger size and more organized structure. Compared to the DF soot, the B20 aggregates have a slightly more compact morphology and smaller primary particle size. No appreciable differences are observed in nanostructure between the DF and B20 soot. The thermogravimetric analysis demonstrates that the B20 soot is associated with lower peak temperature, burnout temperature and apparent activation energy, suggesting that it is more reactive than the DF soot.

Keywords: biodiesel; soot particles; physical property; oxidative reactivity

1. Introduction

Biodiesel fuel (BF) is a renewable alternative to petroleum diesel fuel (DF) and offers many important advantages, including a reasonably similar cetane number and flash point, low-toxicity properties, biodegradability and the requirement of minimal modifications of engine systems [1,2]. In addition, the use of BF is expected to reduce our current dependence on fossil fuels while lowering overall greenhouse gas emissions. For all these reasons, BF has been employed worldwide in diesel-powered vehicles.

Soot particles are an undesirable combustion product of diesel engines, because they are detrimental to the ambient environment and have a variety of adverse health effects [3–5]. The use of BF in diesel engines has been shown to significantly reduce soot emissions [6–10]. Associated with the soot reduction are the changes in the physical and chemical properties of the soot particles, because the physicochemical properties of soot particles are determined by the type of fuel employed and conditions under which the soot is generated [11,12]. The physical properties here include soot morphology and nanostructure, while the chemical properties are based on surface functional groups and metals incorporated into the soot structure. There is presently much interest in the physical and chemical properties of soot particles because they govern the soot reactivity, which is an important factor in the regeneration of diesel particulate filters (DPFs) [13,14]. The DPF is one of the most common technologies used in diesel engines to satisfy stringent regulatory limits on particulate matter emissions.

During engine operation, the DPF in a diesel vehicle must be periodically regenerated by soot oxidation because trapped soot will otherwise clog the unit. Soot reactivity is defined as the ease of soot oxidation. Soot with high reactivity is more readily oxidized, meaning that the temperature required for regeneration of the DPF is lowered.

A considerable number of studies have been performed to explore the impact of the use of BF on the physical properties of soot particles in the diesel engine exhaust stream. It has been reported that the soot aggregates resulting from BF combustion possess more compact morphology and smaller primary particles as compared to those from DF [15,16]. However, analyses of soot nanostructure have produced seemingly contradictory results. As an example, Man et al. [11] and Yehliu et al. [17] found that the exhaust soot from BF combustion exhibited shorter and more curved graphene layers than that from DF. In contrast, Lapuerta et al. [13] and Song et al. [18] reported that the BF soot has a more ordered and graphitic structure. Although many papers have shown the physical properties of BF soot at present, it is difficult to draw a general conclusion on how the BF affects the soot structure based on the obtained data. Therefore, there is still a need for more dedicated studies focusing on the structure of BF soot.

In fact, the use of neat BF involves complications because of several issues, such as high viscosity, high cloud point, low heating value and high cost, and the most practical approach to mitigating these challenges is to blend BF with DF [6,19,20]. A proportion of 20 vol% BF (B20) is recommended by many policy makers and government agencies for use in diesel engines, because this represents a good balance of cost, emission, cold-weather performance, materials compatibility and thermal degradation [2,16,21]. However, to date, there have been few studies assessing the physical properties and reactivity of B20 soot, especially for the soot generated under different engine operating conditions. In the present work, the physical properties and reactivity of both the B20 and DF soot generated at different engine operating loads were studied, using transmission electron microscopy (TEM), Raman spectroscopy (RS) and thermogravimetric (TG) analysis. In addition, the effects of soot's physical properties on reactivity were discussed in detail. The data obtained from this investigation should improve our understanding of the characteristics of BF soot particles and assist in designing DPF for the removal of BF exhaust particles.

2. Materials and Methods

2.1. Engine and Fuels

The experiments were conducted using a four-cylinder in-line diesel engine coupled with an eddy-current dynamometer (AVL ALPHA350AF). A PUMA control system was used to adjust the engine speed and torque. The specifications of the engine are summarized in Table 1. Two diesel fuels were used: an ultralow sulfur diesel without any additives (designated as DF herein) and B20. The B20 fuel was composed of 20% soybean oil methyl ester and 80% DF by volume. The main properties of the DF and B20 are provided in Table 2.

During each test, the cooling water and oil temperatures were maintained within the ranges of 353–358 K and 358–363 K, respectively, and the intake air temperature after turbocharging and intercooling was maintained below 323 K. Tests were conducted under three steady-state operating conditions: 20%, 60% and 100% load at 1600 rpm. To obtain a meaningful comparison, the brake mean effective pressure (BMEP) and injection timing for both DF and B20 trials were kept constant for a given operating mode. Because of the differences in the fuel density and heat value between DF and B20, the injection duration was slightly adjusted to achieve the identical BMEP. The detailed operating conditions are summarized in Table 3.

Table 1. Engine specifications.

Properties	
Bore × Stroke (mm × mm)	102 × 118
Displacement volume (L)	0.964 (single cylinder)
Compression ratio	17:1
Intake system	Turbocharged, intercooled, without exhaust gas recirculation (EGR)
Valves per cylinder	4
Rated power (kW)/speed (rpm)	100/2800
Maximum torque (Nm)/speed (rpm)	400/1500–1700
Injection system	Bosch Common rail
Maximum injection press (MPa)	130
Injector hole diameter (μm)	153

Table 2. Properties of test fuels.

Properties	DF	B20
Sulfur content (μg/g)	42	31
Density (g/mL, 20 °C)	0.838	0.846
Low heating value (MJ/kg)	42.9	41.8
Kinematic viscosity (40 °C, mm^2/s)	4.045	4.654
Flash point (°C)	64	84
50% distillation/°C	247.0	253.2
95% distillation/°C	331.5	333.6
Aromatic content (wt%)	9.8	7.79
Cetane number	51.8	53
% C (wt)	87.2	84.94
% H (wt)	12.8	12.68
% O (wt)	0	2.38

Table 3. Engine operating modes.

Speed (rpm)	Torque (Nm)	Load (%)	BMEP (MPa)
1600	80	20	0.261
1600	240	60	0.782
1600	400	100	1.301

2.2. Soot Sampling Method

The soot samples were harvested from the engine exhaust stream. For collecting soot samples from the hot exhaust, the exhaust gas was diluted by air at a dilution ratio of 10:1 to attain a moderate temperature. The samples for the analysis of soot morphology and nanostructure were deposited onto TEM grids (200 mesh Ni). According to the results of extensive tests, a sampling time of 2–5 min is appropriate for collecting enough soot particles onto the grid and preventing overloading. In addition, Teflon-based filters (PallGelman, R2PL047) were employed to collect particle samples for the RS and TG analyses. The soot particles were dislodged from the filters by ultrasonic wave treatment in dichloromethane, followed by centrifugal separation. This treatment also removed volatile organic compounds (VOCs) from the soot particles. The resulting soot samples without VOCs were dried under nitrogen and then sealed in glass bottles for further analysis.

2.3. Transmission Electron Microscopy

A high-resolution transmission electron microscopy (HRTEM, Philips Tecnai F20) operating at an accelerating voltage of 200 kV with a point resolution of 0.248 nm was used to characterize the soot morphology and nanostructure. The magnification of the TEM instrument was optimized at 20,000×, which allowed the observation of the particles with clear boundaries. TEM images were

digitized to permit calculations of the fractal dimension and the primary particle size using the method proposed by Brasil et al. [22]. For the HRTEM inspection, a magnification of 500,000× was used to observe the nano-scale internal structure of soot's primary particles. Information regarding the soot's nanostructure, including the fringe length (the physical extent of the graphene layer plane), separation distance (the distance between adjacent layer planes) and tortuosity (the ratio of the actual fringe length to the straight-line distance between the endpoint of the carbon layer), were quantified using an automated fringe image processing system. This calculation process was repeated 5 times to determine the measurement uncertainty (standard error). Details regarding the digitizing and analyzing procedures are available in [23].

2.4. Raman Spectroscopy

A Raman scattering spectrometer (Renishaw RM1000) was employed to calculate the graphitization degree of the soot. Spectra were recorded over the range of 900–2000 cm^{-1} with a He-Ne ion laser excitation source operating at 532 nm with power values of 5–6 mW and a spot diameter on the sample of 1.2 μm. For each sample, spectra were obtained at approximately 6 positions with an acquisition time of 10 s. Curve fitting of the Raman spectra was carried out using the peak fitting module in the Origin 9.0 software package.

2.5. Thermogravimetric Analysis

The soot reactivity was estimated using a thermogravimetric analyzer (MettlerToledo TGA/DSC1) with platinum crucibles. Non-isothermal TG trials were conducted in a gas mixture comprising 10% oxygen and 90% N_2 (equivalent to a typical engine exhaust atmosphere) at a flow rate of 50 mL/min. The temperature was increased from 50 to 800 °C at a heating rate of 5 °C/min, and each test was repeated 3 times to ensure reproducibility. The apparent activation energy of each soot sample was calculated based on the TG data using the Mettler-Toledo STARe software (version 9.20) in conjunction with the Friedman method [24].

3. Results and Discussion

3.1. Fractal Morphology

It is well known that diesel exhaust aggregates comprise large numbers of primary particles having various morphological features, including chain, branch and cluster. Aggregates with different shapes and sizes can be characterized by their fractal dimension (D_f), which is widely used to describe the geometric and aerodynamic properties of soot particles. D_f is defined as

$$n = k_f\left(\frac{R_g}{d_p}\right)^{D_f}$$

where n, k_f, R_g and d_p are the number of primary particles per aggregate, the prefactor, the radius of gyration of aggregates and the size of primary particles, respectively. The D_f represents the structural compactness of the aggregate. Theoretically, a smaller D_f suggests aggregates with more chain-like particles, whereas a larger D_f indicates aggregates containing more compact spherical particles. In the present study, D_f values were calculated based on two-dimensional TEM images. Detailed descriptions of the measurement and calculation procedures have been previously reported in [22,25]. For each engine operating mode, approximately 50 aggregates were randomly selected for the D_f calculation to generate sufficient statistics to yield an unbiased result.

Figure 1 plots D_f as a function of BMEP at the medium speed of 1600 rpm. The D_f values are seen to increase monotonically from 1.71 to 1.81 for the DF aggregates and from 1.74 to 1.86 for the B20 aggregates in response to the increased BMEP. The obtained values of D_f are in keeping with results reported in the previous studies on diesel engine exhaust particles [26–28], which are

in the range of 1.6–1.9. As the BMEP increases, the increased in-cylinder temperature and pressure promote soot oxidation. Because the stretched chain-like branches are more readily oxidized than the highly-concentrated core regions [25,29,30], the promotion of soot oxidation results in aggregates with less branches and more compact structure. On the other hand, an increase in the BMEP suggests a decrease in the air–fuel ratio. Such a combustion environment inevitably yields more soot particles, which enhances the frequency of collisions among particles and so generates aggregates with more compact morphology [27].

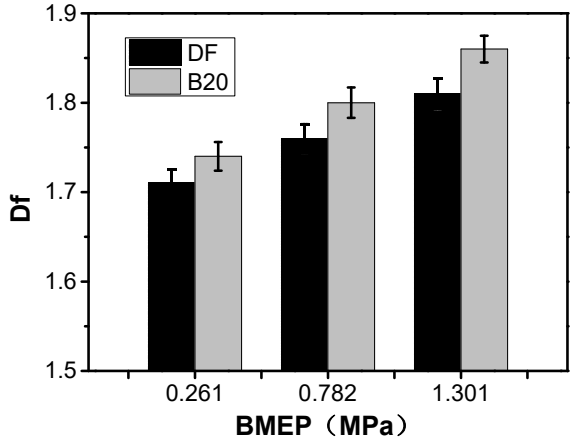

Figure 1. Fractal dimension (Df) values of soot particles as a function of BMEP.

Figure 1 demonstrates that at the same engine load, the D_f value for the DF aggregates is somewhat smaller than that for the B20 aggregates. This result indicates that the DF produces more aggregates with chain-like branches than the B20, as also evidenced by the TEM images of diesel particles in Figure 2. Similar findings were reported by Savic et al. [16], who determined that the aggregates have a slight tendency towards having a smaller size and more compact morphology when increasing the biodiesel content in blended fuel. This phenomenon can be explained by focusing on the oxygen content of biodiesel, which promotes soot oxidation and facilitates the generation of small particles with shorter chains [15]. In addition, the exhaust particles from biodiesel fuel generally contain more VOCs than those obtained from diesel fuel [31–33]. These VOCs condense on the particles and fill in the voids of the aggregates, thereby making the aggregates more compact [26,34].

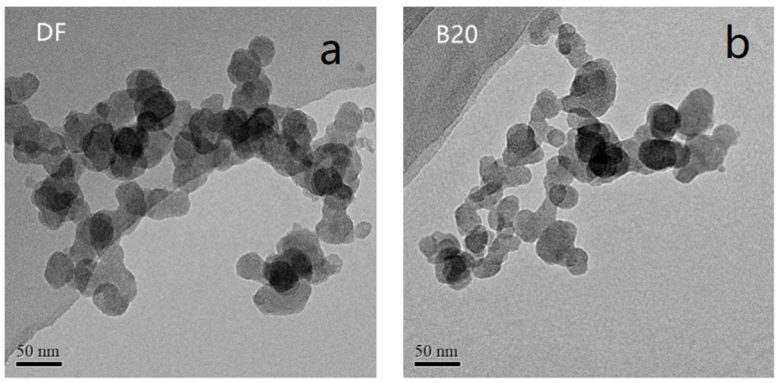

Figure 2. Typical TEM images of particles sampled at BMEP = 0.782 MPa: (**a**) DF, (**b**) B20.

3.2. Primary Particle Size

More than 300 spherules with clear boundaries from different aggregates in the TEM images were randomly selected to determine the primary particle size (d_p), based on a procedure previously reported in [25,27]. Figure 3 presents the d_p distributions for both the DF and B20 soot particles.

Based on multiple digitizations of the TEM images, the measurement uncertainty for the mean values of dp was also obtained. The Gaussian fits are overlaid on the histograms as probability density functions (PDFs). Because the description of the distribution using a cursorily-picked threshold will lead to a subjective result, the dp distributions are characterized using the third quantile (75%), which is often used to describe data distribution in statistics. For the DF soot particles, 75% of the primary particles are smaller than 23.37 nm at the BMEP of 0.261 MPa, 26.91 nm at the BMEP of 0.782 MPa and 29.53 nm at the BMEP of 1.301 MPa. In the case of the B20 soot particles, the corresponding values are 23.32, 26.89 and 28.73 nm, respectively. The mean primary particle diameters ($\overline{d_p}$) increase from 19.69 to 24.17 nm for the DF soot and from 19.51 to 23.75 nm for the B20 soot when increasing the BMEP from 0.261 to 1.301 MPa. In a study by Neel et al. [27] concerning diesel exhaust soot particles, $\overline{d_p}$ is also found to increase along with the engine load. Neel concluded that the primary particle size was highly correlated with the air–fuel ratio. Theoretically, the air–fuel ratio for a diesel engine shows an approximately inverse proportionality to the engine load. Thus, with increase in the engine load, the decreased air–fuel ratio would be expected to promote soot nucleation and growth, resulting in an increase in the primary particle size.

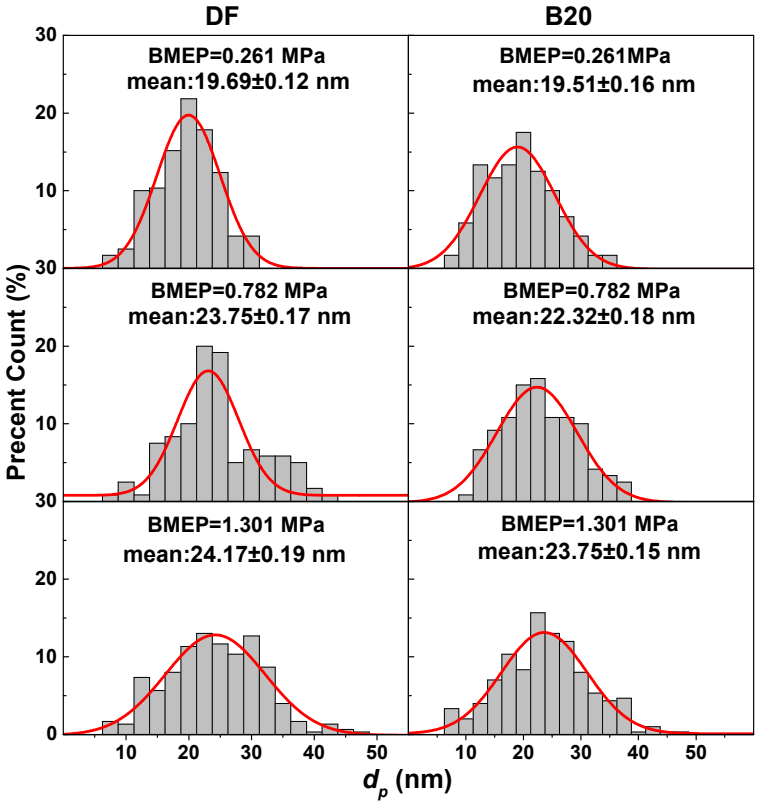

Figure 3. Distributions of primary particle size (d_p) for both DF and B20 soot in the various test modes.

Previous investigations reported that using biodiesel fuel reduces the primary particles' size [13,16], and similar results were obtained in the present work. Because only 20 vol.% BF was used in the blend, the B20 soot shows only slightly lower $\overline{d_p}$ values at the same engine load, as indicated in Figure 3. This reduction in the primary particle size can be attributed to three factors. Firstly, the presence of oxygen in the biodiesel improves the local air–fuel ratio, thus promoting soot oxidation [7,35]. Secondly, the lower concentration of carbon in the biodiesel slows the surface growth rate of soot particles [36]. Lastly, the high oxidative reactivity of biodiesel particles causes shrinkage of particles [8].

3.3. Nanostructure

HRTEM was used to identify the internal structure of the soot particles and Figure 4 presents typical HRTEM images of the exhaust soot particles generated from combustion of the DF and B20. The primary particles are seen to comprise an inner amorphous core and an outer portion that can be distinguished by numerous distinct graphene lamellae. In addition, the contour of B20 soot is generally more nebulous and irregular than that of the DF soot. To clearly depict the characteristics of soot nanostructure, approximately 100 primary soot particles from different aggregates in each soot sample were randomly selected to perform a quantitative analysis of nanostructure parameters, including the fringe length (L_a), separation distance (d_s) and tortuosity (T_f).

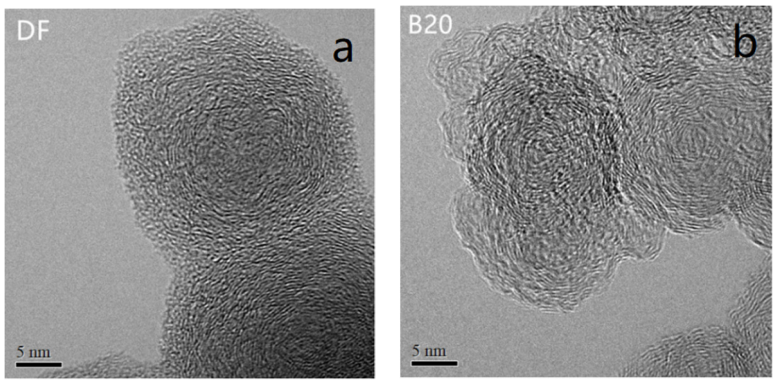

Figure 4. Typical HRTEM images of diesel particles sampled at BMEP = 0.782 MPa: (**a**) DF, (**b**) B20.

The distribution histograms of L_a, d_s and T_f for both DF and B20 soot are provided in Figures 5–7. The PDFs overlaid on the distribution histograms follow a lognormal distribution, and are nearly monodispersed. For a given test mode, the L_a, d_s and T_f values for both soots are within the ranges of 0.2–5.0 nm, 0.30–0.46 nm and 1.0–1.8 respectively. As a general observation, it is difficult to establish any clear trends concerning the structural differences. Thus, the mean values of L_a ($\overline{L_a}$), d_s ($\overline{d_s}$) and T_f ($\overline{T_f}$) were used to characterize the soot nanostructure. It can be seen from Figures 5–7 that both the DF and B20 soot show an increase in $\overline{L_a}$ but decreases in $\overline{d_s}$ and $\overline{T_f}$ with an increase in BMEP, indicating that the soot particles evolve toward a more ordered structure. Zhu et al. [25] assessed the physical properties of light-duty diesel engine particles, and also found that the soot nanostructure became more ordered when increasing the engine load. Combustion condition is an important factor governing soot nanostructure [23,37]. At a given engine speed, the increased engine load means an increase in combustion temperature. The elevated temperature promotes the decomposition of the fuel into smaller molecular precursors, resulting in the formation of more ordered carbon layers in the soot particles [37,38]. On the other hand, the high temperature provides sufficient thermal activation to surmount the activation energy required for growth and reorientation of the carbon lamella, and as a consequence, promotes the growth of crystallites [39,40].

Another factor governing soot nanostructure is the fuel property [11,12]. Man et al. [11] reported that the exhaust soot particles from neat biodiesel were 10–16% shorter in $\overline{L_a}$ and 8–11% larger in $\overline{T_f}$ than those produced from DF. However, our results indicate that the differences in $\overline{L_a}$, $\overline{d_s}$ and $\overline{T_f}$ between the B20 and DF soot are only less than 2% at the same engine load, likely due to the relatively low proportion of biodiesel in the fuel. Considering the measurement uncertainties, it is evident that there is no significant impact on soot nanostructure when adding 20 vol.% biodiesel into the diesel.

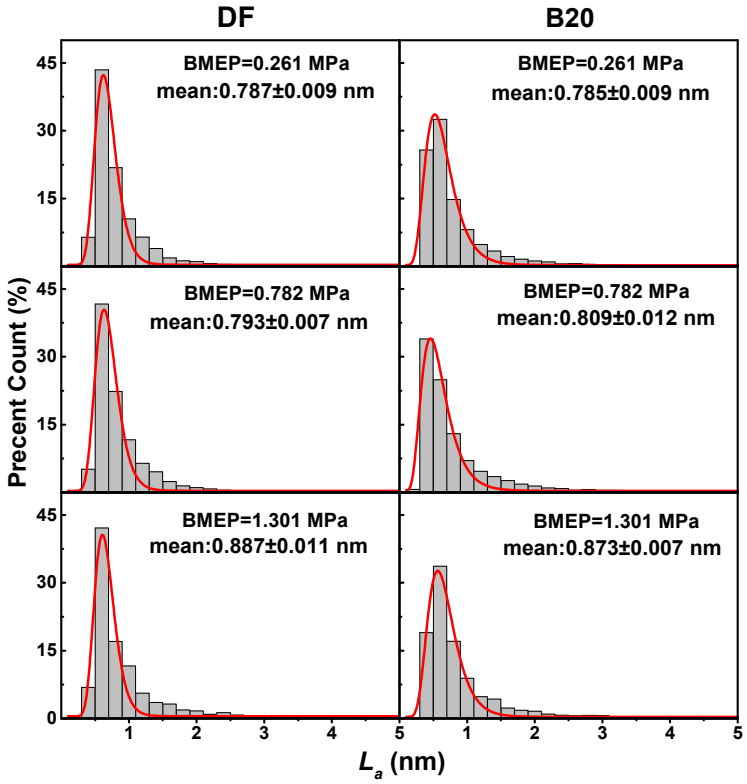

Figure 5. Histograms of fringe length (L_a) data for both DF and B20 soot in the applied test modes.

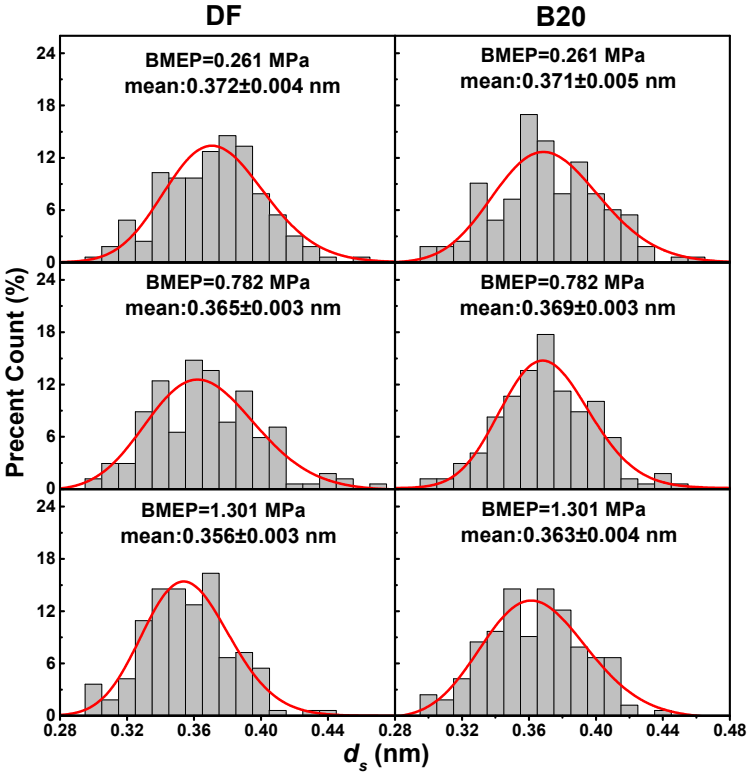

Figure 6. Histograms of separation distance (d_s) data for both DF and B20 soot in the applied test modes.

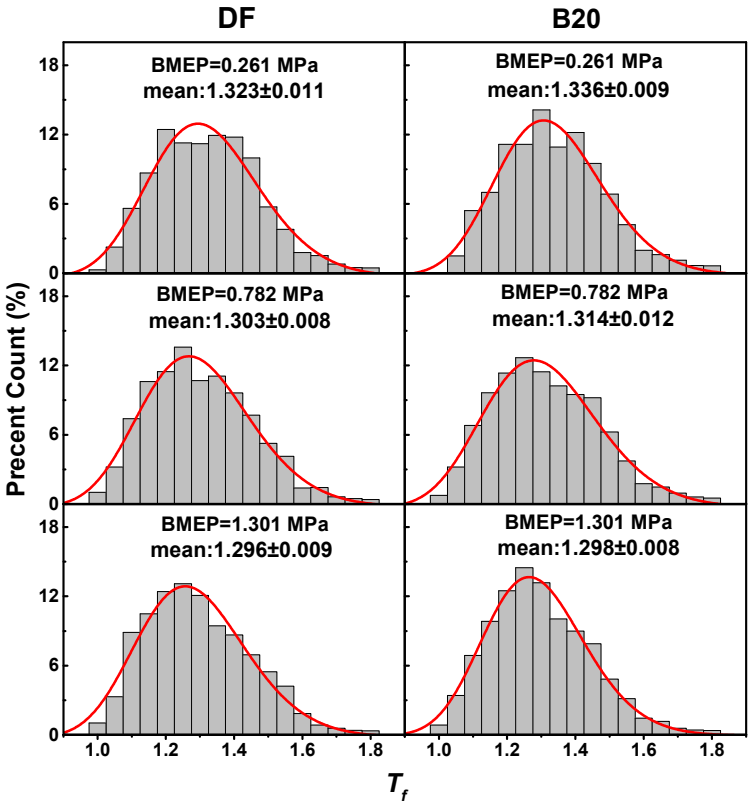

Figure 7. Histograms of tortuosity (T_f) for both DF and B20 soot in the applied test modes.

3.4. Soot Graphitization Degree

RS analysis was used to support the soot nanostructure results, because this technique can provide information regarding the graphitization degree of soot particles. According to the method proposed by Sadezky et al. [41], the Raman spectra of the soot were resolved into three Lorentzian bands at approximately 1200 (D4), 1345 (D1), and 1580 cm^{-1} (G) together with one Gaussian-shaped band at about 1520 cm^{-1} (D3). This process was repeated 5 times for each spectrum to ensure the reliability of the curve fitting procedure, and the uncertainty of spectral parameters determined by curve fitting was found to be less than 4%. The D1 band corresponds to the disordered structure at the edges of graphene layers and crystalline defects, while the G peak reflects the graphitic lattice. Thus, the ratio of the D1 peak area to that of the G peak (A_{D1}/A_G) is employed to characterize the graphitization degree of the soot particles [25,42].

As the BMEP increases from 0.261 to 1.301 MPa, the A_{D1}/A_G values in Figure 8 decrease from 2.348 to 1.880 for the DF soot and from 2.355 to 1.898 for the B20 soot, indicating an increased graphitization degree. These changes are in agreement with the information obtained from the analysis of HRTEM images, and confirm that the soot nanostructure becomes more ordered with the increase in the engine load. Close inspection of Figure 8 confirms that the differences in the A_{D1}/A_G values between B20 and DF soot are less than 2.7% at the same engine load. These RS results therefore support the assertion derived from the HRTEM analysis that there are no significant differences in nanostructure between the DF and B20 soot.

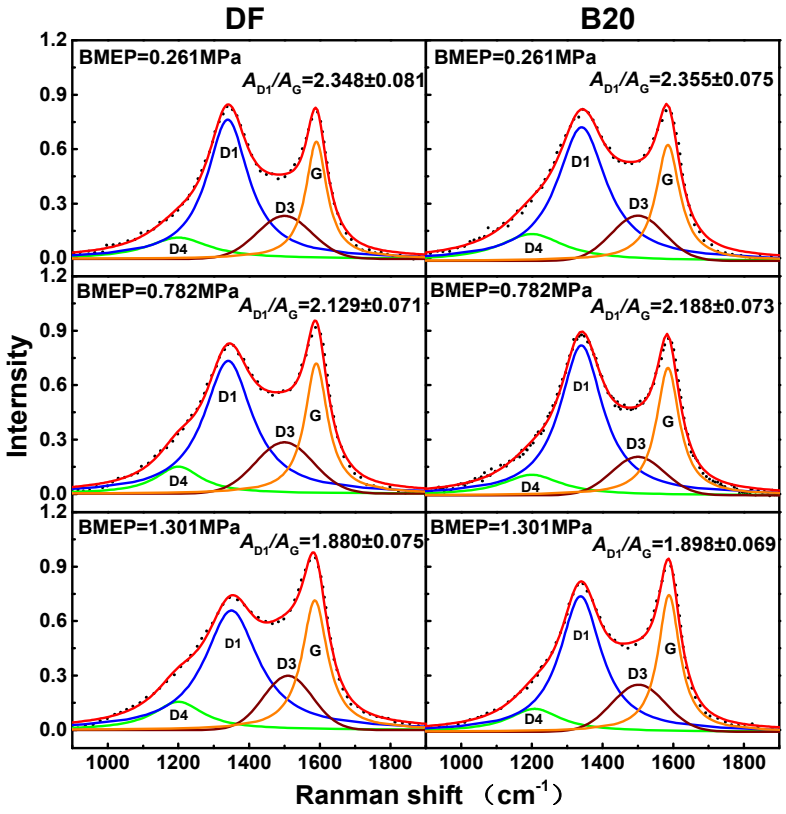

Figure 8. Raman spectroscopy analysis for the DF and B20 soot under test working conditions.

3.5. Soot Reactivity

Soot reactivity was characterized by TG analysis, and Figure 9 presents the typical smoothed TG-differential thermogravimetry (DTG) profiles of the DF and B20 soot. From the TG and DTG curves, the oxidation kinetic parameters were determined, including the peak temperature (T_p), burnout temperature (T_b) and apparent activation energy (E_a). Here, T_p refers to the temperature at which the maximum rate of mass loss occurs, such that a lower T_p suggests easier ignition. Tb represents the temperature at which the oxidation of the soot is complete. The E_a was calculated through the Arrhenius-type reaction model, which is described as below:

$$-\frac{dm}{dt} = Aexp(\frac{-Ea}{RT})m^n {p_{O_2}}^r$$

where the m, t and p_{O_2} refer to the sample mass, time, and partial pressure of oxygen, respectively. A is the pre-exponential factor, R is the universal gas constant and T is the temperature. The parameters n and r are the reaction orders of sample and oxygen, respectively. The calculation procedures for the kinetic parameters have been described in detail in [24,43].

Table 4 shows that the T_p, T_b and E_a values for both the DF and B20 soot increase along with BMEP, suggesting a decrease in soot reactivity. Man et al. [11] investigated the effects of biodiesel on the properties of particles from a direct-injection diesel engine. They found that soot generated at low engine load shows higher reactivity than soot generated at high engine load when using neat diesel, biodiesel and their blends, in agreement with our results.

It is believed that soot reactivity depends essentially on its physico-chemical properties, including morphology, nanostructure, and chemical composition. For instance, aggregates with small Df and primary particle size will have relatively large specific surface areas, which provide more active sites for oxygen attack and thereby the soot reactivity is enhanced [34,44]. With regard to nanostructure, a shorter fringe suggests a greater proportion of carbon atoms at the edge-sites of graphene layers.

Compared to the carbon atoms in the basal plane, the edge carbon atoms more readily form bonds with chemisorbed oxygen and are more accessible to oxidizers [45]. Higher tortuosity means that more odd-membered rings are within the carbon planes and/or more sp^3 carbon atoms present in the sp^2 carbon framework. Odd-membered rings or sp^3 hybridized carbon atoms are more susceptible to oxidative attack than hexagonal rings containing only sp^2 hybridized carbon, reflecting less electron resonance stabilization [46]. In this study, the increased engine load increases D_f, d_p and L_a while decreasing T_f and ds for both the DF and B20 soot, which in turn contribute to reduction in soot reactivity.

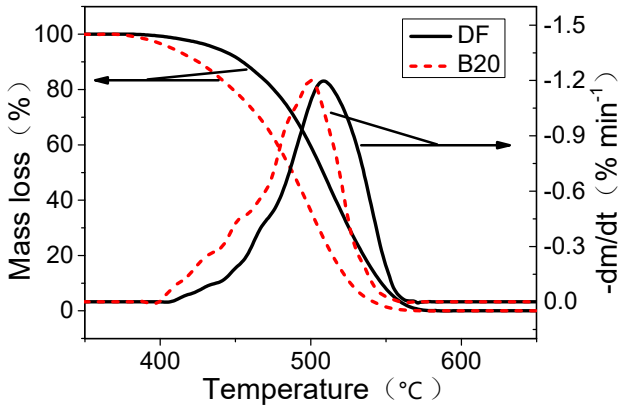

Figure 9. Typical TG and DTG profiles obtained from the soot sampled at BMEP = 0.782 MPa.

Table 4. Peak temperature (T_p), burnout temperature (T_b) and apparent activation energy (E_a) for soot samples.

BMEP	DF			B20		
	T_p (°C)	T_b (°C)	E_a (kJ/mol)	T_p (°C)	T_b (°C)	E_a (kJ/mol)
0.261 MPa	505.8	532.6	144.2	483.7	498.8	134.3
0.782 MPa	510.5	546.7	154.5	500.2	526.8	142.9
1.301 MPa	566.5	607.3	163.9	519.8	550.2	154.6

The standard errors are within 2.0 °C for T_p and T_b, and 1.2 kJ/mol for E_a.

At the same engine loads, as seen from Table 4, the B20 soot has higher reactivity than the DF soot. This behavior seems to be inconsistent with the morphology and nanostructure results, which establish that both DF and B20 soot have almost identical values in terms of D_f, d_p, L_a, T_f and d_s at the same engine load. In fact, soot reactivity depends not only on physical properties but also on chemical properties. Song et al. [18,47] examined the oxidation behavior of BF soot, and found that BF soot possessed more surface oxygen groups than DF soot. They concluded that there is a positive correlation between the concentration of surface oxygen groups and reactivity. Li et al. [33] investigated the effect of the diesel/biodiesel blend ratio on soot oxidative reactivity, and argued that the addition of biodiesel increases the quantity of aliphatic C–H groups on the soot surface. These aliphatic C–H groups are an important factor governing soot oxidative reactivity [34,48]. In addition, the metallic species in soot can act as catalysts and strongly affect soot reactivity [49,50]. Because of the use of KOH and NaOH as catalysts in the transesterification process during biodiesel production, the Na and K contents in BF soot are much higher than those in DF soot [3,51]. The relatively high contents of K and Na can accelerate soot oxidation, and as a consequence, improve soot reactivity. Because of our focus on the physical properties of soot particles, no information concerning chemical properties is provided in this paper. Even so, considering the almost identical physical properties of the DF and B20 soot, it is likely that the different reactivity between the DF and B20 soot can be primarily ascribed to variations in the chemical properties of the soot.

4. Conclusions

The physical properties and oxidative reactivity of soot particles generated from the combustion of B20 and DF were studied at different engine loads. With increases in the engine load, both the B20 and DF soot particles tend to become more compact in morphology and larger in primary particle size. Nanostructural analysis of both soots shows an increase in the fringe length and decreases in the separation distance and tortuosity, suggesting a transformation toward a more disordered structure. At the same engine load, the B20 soot is marginally larger in the compactness of aggregate and slightly smaller in the primary particle size than the DF soot. Furthermore, no significant differences in nanostructure were identified between the B20 and DF soot, because the values of fringe length, separation distance and tortuosity are almost the same for both soots. This assertion is evidenced by the results of Raman spectroscopy analysis, where the graphitization degree of both soots is nearly identical.

Thermogravimetric analysis demonstrates that the peak temperature, burnout temperature and apparent activation energy for both the B20 and DF soot increase along with the engine load, indicating a decrease in the oxidative reactivity. At the same engine load, the B20 soot exhibits greater oxidative reactivity than the DF soot because it has relatively lower values for peak temperature, burnout temperature and apparent activation energy. Considering that there are no significant differences in the physical properties between the B20 and DF soot, it is possible that the chemical properties of the B20 soot are responsible for its higher reactivity.

Author Contributions: Conceptualization, X.Z. and C.S.; methodology, G.L., C.S. and Y.Q.; software, X.Z. and Y.Q.; validation, X.Z. and Y.Q.; formal analysis, X.Z.; investigation, X.Z. and Y.Q.; resources, G.L. and C.S.; writing—original draft preparation, X.Z. and G.L.; writing—review and editing, X.Z., G.L. and C.S.; supervision, C.S.; funding acquisition, G.L. and C.S. All authors have read and agreed to the published version of the manuscript.

Funding: This research was funded by the National Natural Science Foundation of China (No. 51876142) and the Program of Tianjin Science and Technology Plan (18PTZWHZ00170).

Conflicts of Interest: The authors declare no conflict of interest.

References

1. European Commission. Directive 2009/28/EC, on the promotion of the use of energy from renewable sources and amending and subsequently repealing directives 2001/77/EC and 2003/30/EC. *Off. J. Eur. Union* **2009**, *140*, 16–62.
2. Can, Ö.; Öztürk, E.; Solmaz, H.; Aksoy, F.; Çinar, C.; Yücesu, H.S. Combined effects of soybean biodiesel fuel addition and EGR application on the combustion and exhaust emissions in a diesel engine. *Appl. Therm. Eng.* **2016**, *95*, 115–124. [CrossRef]
3. Wang, Y.; Liu, H.; Lee, C.-F.F. Particulate matter emission characteristics of diesel engines with biodiesel or biodiesel blending: A review. *Renew. Sustain. Energy Rev.* **2016**, *64*, 569–581. [CrossRef]
4. Sakhare, N.M.; Shelke, P.S.; Lahane, S. Experimental Investigation of Effect of Exhaust Gas Recirculation and Cottonseed B20 Biodiesel Fuel on Diesel Engine. *Procedia Technol.* **2016**, *25*, 869–876. [CrossRef]
5. Cassee, F.R.; Heroux, M.E.; Gerlofs-Nijland, M.E.; Kelly, F.J. Particulate matter beyond mass: Recent health evidence on the role of fractions, chemical constituents and sources of emission. *Inhal. Toxicol.* **2013**, *25*, 802–812. [CrossRef] [PubMed]
6. Bueno, A.V.; Pereira, M.P.B.; De Oliveira Pontes, J.V.; De Luna, F.M.T.; Cavalcante, C.L. Performance and emissions characteristics of castor oil biodiesel fuel blends. *Appl. Therm. Eng.* **2017**, *125*, 559–566. [CrossRef]
7. Lapuerta, M.; Armas, O.; Rodriguez-Fernandez, J. Effect of biodiesel fuels on diesel engine emissions. *Prog. Energy Combust. Sci.* **2008**, *34*, 198–223. [CrossRef]
8. Salamanca, M.; Mondragón, F.; Agudelo, J.R.; Benjumea, P.; Santamaría, A. Variations in the chemical composition and morphology of soot induced by the unsaturation degree of biodiesel and a biodiesel blend. *Combust. Flame* **2012**, *159*, 1100–1108. [CrossRef]

9. Alagu, K.; Venu, H.; Jayaraman, J.; Raju, V.D.; Subramani, L.; Appavu, P. Novel water hyacinth biodiesel as a potential alternative fuel for existing unmodified diesel engine: Performance, combustion and emission characteristics. *Energy* **2019**, *179*, 295–305. [CrossRef]
10. Wei, L.; Cheung, C.S.; Ning, Z. Influence of waste cooking oil biodiesel on combustion, unregulated gaseous emissions and particulate emissions of a direct-injection diesel engine. *Energy* **2017**, *127*, 175–185. [CrossRef]
11. Man, X.J.; Cheung, C.S.; Ning, Z.; Yung, K.F. Effect of Waste Cooking Oil Biodiesel on the Properties of Particulate from a DI Diesel Engine. *Aerosol Sci. Technol.* **2015**, *49*, 199–209. [CrossRef]
12. Vander Wal, R.L.; Tomasek, A.J. Soot oxidation: Dependence upon initial nanostructure. *Combust. Flame* **2003**, *134*, 1–9. [CrossRef]
13. Lapuerta, M.; Oliva, F.; Agudelo, J.R.; Boehman, A.L. Effect of fuel on the soot nanostructure and consequences on loading and regeneration of diesel particulate filters. *Combust. Flame* **2012**, *159*, 844–853. [CrossRef]
14. Choi, S.; Seong, H. Oxidation characteristics of gasoline direct-injection (GDI) engine soot: Catalytic effects of ash and modified kinetic correlation. *Combust. Flame* **2015**, *162*, 2371–2389. [CrossRef]
15. Verma, P.; Pickering, E.; Jafari, M.; Guo, Y.; Stevanovic, S.; Fernando, J.F.S. Influence of fuel-oxygen content on morphology and nanostructure of soot particles. *Combust. Flame* **2019**, *205*, 206–219. [CrossRef]
16. Savic, N.; Rahman, M.M.; Miljevic, B.; Saathoff, H.; Naumann, K.H.; Leisner, T. Influence of biodiesel fuel composition on the morphology and microstructure of particles emitted from diesel engines. *Carbon* **2016**, *104*, 179–189. [CrossRef]
17. Yehliu, K.; Vander Wal, R.L.; Armas, O.; Boehman, A.L. Impact of fuel formulation on the nanostructure and reactivity of diesel soot. *Combust. Flame* **2012**, *159*, 3597–3606. [CrossRef]
18. Song, J.; Alam, M.; Boehman, A.L. Impact of Alternative Fuels on Soot Properties and DPF Regeneration. *Combust. Sci. Technol.* **2007**, *179*, 1991–2037. [CrossRef]
19. Merchan-Merchan, W.; Abdihamzehkolaei, A.; Merchan-Breuer, D.A. Formation and evolution of carbon particles in coflow diffusion air flames of vaporized biodiesel, diesel and biodiesel-diesel blends. *Fuel* **2018**, *226*, 263–277. [CrossRef]
20. Jeon, J.; Park, S. Effect of injection pressure on soot formation/oxidation characteristics using a two-color photometric method in a compression-ignition engine fueled with biodiesel blend (B20). *Appl. Therm. Eng.* **2018**, *131*, 284–294. [CrossRef]
21. Chen, H.; He, J.; Chen, Y.; Hua, H. Performance of a common rail diesel engine using biodiesel of waste cooking oil and gasoline blend. *J. Energy Inst.* **2018**, *91*, 856–866. [CrossRef]
22. Brasil, A.M.; Farias, T.L.; Carvalho, M.G. A recipe for image characterization of fractal-like aggregates. *J. Aerosol Sci.* **1999**, *30*, 1379–1389. [CrossRef]
23. Li, Z.; Song, C.; Song, J.; Lv, G.; Dong, S.; Zhao, Z. Evolution of the nanostructure, fractal dimension and size of in-cylinder soot during diesel combustion process. *Combust. Flame* **2011**, *158*, 1624–1630. [CrossRef]
24. Friedman, H.L. New methods for evaluating kinetic parameters from thermal analysis data. *J. Polym. Sci. Part B Polym. Lett.* **1969**, *7*, 41–46. [CrossRef]
25. Zhu, J.; Lee, K.O.; Yozgatligil, A.; Choi, M.Y. Effects of engine operating conditions on morphology, microstructure, and fractal geometry of light-duty diesel engine particulates. *Proc. Combust. Inst.* **2005**, *30*, 2781–2789. [CrossRef]
26. Chandler, M.F.; Teng, Y.; Koylu, U.O. Diesel engine particulate emissions: A comparison of mobility and microscopy size measurements. *Proc. Combust. Inst.* **2007**, *31*, 2971–2979. [CrossRef]
27. Neer, A.; Koylu, U. Effect of operating conditions on the size, morphology, and concentration of submicrometer particulates emitted from a diesel engine. *Combust. Flame* **2006**, *146*, 142–154. [CrossRef]
28. Gaddam, C.K.; Vander Wal, R.L. Physical and chemical characterization of SIDI engine particulates. *Combust. Flame* **2013**, *160*, 2517–2528. [CrossRef]
29. Ruiz, F.A.; Cadrazco, M.; López, A.F.; Sanchez-Valdepeñas, J.; Agudelo, J.R. Impact of dual-fuel combustion with n-butanol or hydrous ethanol on the oxidation reactivity and nanostructure of diesel particulate matter. *Fuel* **2015**, *161*, 18–25. [CrossRef]
30. Zhang, R.; Kook, S. Structural evolution of soot particles during diesel combustion in a single-cylinder light-duty engine. *Combust. Flame* **2015**, *162*, 2720–2728. [CrossRef]
31. Hwang, J.; Hirner, F.S.; Bae, C.; Patel, C.; Gupta, T.; Agarwal, A.K. HRTEM evaluation of primary soot particles originated in a small-bore biofuel compression-ignition engine. *Appl. Therm. Eng.* **2019**, *159*, 113899. [CrossRef]

32. Qu, L.; Wang, Z.; Zhang, J. Influence of waste cooking oil biodiesel on oxidation reactivity and nanostructure of particulate matter from diesel engine. *Fuel* **2016**, *181*, 389–395. [CrossRef]
33. Li, R.; Wang, Z. Study on status characteristics and oxidation reactivity of biodiesel particulate matter. *Fuel* **2018**, *218*, 218–226. [CrossRef]
34. Agudelo, J.R.; Álvarez, A.; Armas, O. Impact of crude vegetable oils on the oxidation reactivity and nanostructure of diesel particulate matter. *Combust. Flame* **2014**, *161*, 2904–2915. [CrossRef]
35. Lapuerta, M.; Armas, O.; Hernández, J.J.; Tsolakis, A. Potential for reducing emissions in a diesel engine by fuelling with conventional biodiesel and Fischer-Tropsch diesel. *Fuel* **2010**, *89*, 3106–3113. [CrossRef]
36. Stanmore, B.R.; Brilhac, J.F.; Gilot, P. The oxidation of soot: A review of experiments, mechanisms and models. *Carbon* **2001**, *39*, 2247–2268. [CrossRef]
37. Xu, Z.; Li, X.; Guan, C.; Huang, Z. Effects of injection timing on exhaust particle size and nanostructure on a diesel engine at different loads. *J. Aerosol Sci.* **2014**, *76*, 28–38. [CrossRef]
38. Alfè, M.; Apicella, B.; Barbella, R.; Rouzaud, J.N.; Tregrossi, A.; Ciajolo, A. Structure-property relationship in nanostructures of young and mature soot in premixed flames. *Proc. Combust. Inst.* **2009**, *32*, 697–704. [CrossRef]
39. Vander Wal, R.L.; Tomasek, A.J. Soot nanostructure: Dependence upon synthesis conditions. *Combust. Flame* **2004**, *136*, 129–140. [CrossRef]
40. Al-Qurashi, K.; Boehman, A.L. Impact of exhaust gas recirculation (EGR) on the oxidative reactivity of diesel engine soot. *Combust. Flame* **2008**, *155*, 675–695. [CrossRef]
41. Sadezky, A.; Muckenhuber, H.; Grothe, H.; Niessner, R.; Pöschl, U.J.C. Raman microspectroscopy of soot and related carbonaceous materials: Spectral analysis and structural information. *Carbon* **2005**, *43*, 1731–1742. [CrossRef]
42. Gaddam, C.K.; Vander Wal, R.L.; Chen, X.; Yezerets, A.; Kamasamudram, K. Reconciliation of carbon oxidation rates and activation energies based on changing nanostructure. *Carbon* **2016**, *98*, 545–556. [CrossRef]
43. Zhang, D.; Ma, Y.; Zhu, M. Nanostructure and oxidative properties of soot from a compression ignition engine: The effect of a homogeneous combustion catalyst. *Proc. Combust. Inst.* **2013**, *34*, 1869–1876. [CrossRef]
44. Mühlbauer, W.; Zöllner, C.; Lehmann, S.; Lorenz, S.; Brüggemann, D. Correlations between physicochemical properties of emitted diesel particulate matter and its reactivity. *Combust. Flame* **2016**, *167*, 39–51. [CrossRef]
45. Zhang, Y.; Boehman, A.L. Oxidation behavior of soot generated from the combustion of methyl 2-butenoate in a co-flow diffusion flame. *Combust. Flame* **2013**, *160*, 112–129. [CrossRef]
46. Randy, L.; Vander Wal, C.J.M. Initial Investigation of Effects of Fuel Oxygenation on Nanostructure of Soot from a Direct-Injection Diesel Engine. *Energy Fuels* **2006**, *20*, 2364–2369. [CrossRef]
47. Song, J.; Alam, M.; Boehman, A.; Kim, U. Examination of the oxidation behavior of biodiesel soot. *Combust. Flame* **2006**, *146*, 589–604. [CrossRef]
48. Wang, L.; Song, C.; Song, J.; Lv, G.; Pang, H.; Zhang, W. Aliphatic C-H and oxygenated surface functional groups of diesel in-cylinder soot: Characterizations and impact on soot oxidation behavior. *Proc. Combust. Inst.* **2013**, *34*, 3099–3106. [CrossRef]
49. Ess, M.N.; Bladt, H.; Mühlbauer, W.; Seher, S.I.; Zöllner, C.; Lorenz, S. Reactivity and structure of soot generated at varying biofuel content and engine operating parameters. *Combust. Flame* **2015**, *167*, 39–51. [CrossRef]
50. Bladt, H.; Schmid, J.; Kireeva, E.D.; Popovicheva, O.B.; Perseantseva, N.M.; Timofeev, M.A. Impact of Fe Content in Laboratory-Produced Soot Aerosol on its Composition, Structure, and Thermo-Chemical Properties. *Aerosol Sci. Technol.* **2012**, *46*, 1337–1348. [CrossRef]
51. Dubey, P.; Gupta, R. Effects of dual bio-fuel (Jatropha biodiesel and turpentine oil) on a single cylinder naturally aspirated diesel engine without EGR. *Appl. Therm. Eng.* **2017**, *115*, 1137–1147. [CrossRef]